Development of a discrete gas-kinetic scheme for simulation of two-dimensional viscous incompressible and compressible flows

L. M. Yang,[1] C. Shu,[2,*] and Y. Wang[2]

[1]*Department of Aerodynamics, College of Aerospace Engineering, Nanjing University of Aeronautics and Astronautics, Yudao Street, Nanjing 210016, Jiangsu, China*

[2]*Department of Mechanical Engineering, National University of Singapore, 10 Kent Ridge Crescent, Singapore 119260*

(Received 21 November 2015; revised manuscript received 24 February 2016; published 23 March 2016)

In this work, a discrete gas-kinetic scheme (DGKS) is presented for simulation of two-dimensional viscous incompressible and compressible flows. This scheme is developed from the circular function-based GKS, which was recently proposed by Shu and his co-workers [L. M. Yang, C. Shu, and J. Wu, J. Comput. Phys. **274**, 611 (2014)]. For the circular function-based GKS, the integrals for conservation forms of moments in the infinity domain for the Maxwellian function-based GKS are simplified to those integrals along the circle. As a result, the explicit formulations of conservative variables and fluxes are derived. However, these explicit formulations of circular function-based GKS for viscous flows are still complicated, which may not be easy for the application by new users. By using certain discrete points to represent the circle in the phase velocity space, the complicated formulations can be replaced by a simple solution process. The basic requirement is that the conservation forms of moments for the circular function-based GKS can be accurately satisfied by weighted summation of distribution functions at discrete points. In this work, it is shown that integral quadrature by four discrete points on the circle, which forms the D2Q4 discrete velocity model, can exactly match the integrals. Numerical results showed that the present scheme can provide accurate numerical results for incompressible and compressible viscous flows with roughly the same computational cost as that needed by the Roe scheme.

DOI: 10.1103/PhysRevE.93.033311

I. INTRODUCTION

In recent years, as a promising alternative computational fluid dynamics (CFD) approach, the gas-kinetic scheme (GKS) has received increasing attention and made a lot of achievements in various fields, such as in incompressible flows [1–3], compressible flows [4–7], rarefied flows [8–10], turbulence flows [11,12], etc. In GKS, the finite volume method (FVM) or the finite difference method (FDM) is usually applied to discretize the macroscopic governing equations and the local solution of the Boltzmann equation is utilized to compute the fluxes of conservative variables at the cell interface. Since the numerical fluxes are obtained from the local solution of physical equation instead of numerical approximation, the solution of GKS is more credible. In particular, for the supersonic and hypersonic flows, GKS captures strong shock waves stably without the "carbuncle phenomenon" [13,14].

To date, there are lots of studies on the GKS. Some of them include the work of Pullin [15], Mandal and Deshpande [16], Chou and Baganoff [17], Yang *et al.* [18], Xu [19,20], Chae *et al.* [21], Jiang and Qian [22], Sun *et al.* [23], Shu and his co-workers [24,25], and Ohwada and his co-workers [26–28]. Among them, those methods reported in [15–17] can be classified as the kinetic flux vector splitting (KFVS) scheme. Basically, for the KFVS scheme, the collisionless Boltzmann equation is solved in the gas evolution stage, and the collision process is controlled by a numerical time step. As a result, the KFVS scheme provides good positivity property for simulation of flows with strong shock wave and expansion wave, but gives poorer results than those obtained from the Harten-Lax-van Leer (HLL) scheme [29] and the Roe scheme [30]. With inclusion of the Bhatnagar-Gross-Krook (BGK) collision model during the gas evolution stage, the gas-kinetic BGK scheme was proposed and developed in recent decades [19–22]. For the gas-kinetic BGK scheme, the dissipation in the streaming process is controlled by the collision time rather than by the numerical time step. Therefore, the gas-kinetic BGK scheme usually works very well for both incompressible and compressible flows. To construct a general gas-kinetic scheme, Ohwada [26] proposed a railroad method, with which the theoretical backgrounds of the KFVS scheme and the gas-kinetic BGK scheme can be well unified. Furthermore, Ohwada and Kobayashi [27] systematically studied the influence of various reconstruction methods on the kinetic scheme and developed several robust gas-kinetic schemes.

On the other hand, it is indicated that the gas-kinetic equation with the Maxwellian distribution function [15–17,19–23,26,27] or the general distribution function [18] is usually used to calculate the numerical fluxes at the cell interface in most of the GKS. Due to the complexity of the Maxwellian function and the general distribution function, these schemes are usually more complicated and less efficient than the traditional Riemann solvers [29–31]. In addition, as pointed out in [7], for the viscous flow simulated by the GKS [19–22] it is required to calculate a number of coefficients related to the physical space and phase space at every cell interface and each time step. This makes the evaluation of numerical fluxes by the GKS expensive. To improve the computational efficiency of the Maxwellian function-based GKS and simplify its derivation, the circular function-based GKS for the two-dimensional case is developed by Shu and his co-workers [24,25]. In the method, it assumes that the mass, momentum, and energy of particles in the phase velocity

*mpeshuc@nus.edu.sg

space are concentrated on a circle. Thus, the integrals for conservation forms of moments in the infinity domain for the Maxwellian function-based GKS, which are needed to recover Navier-Stokes equations, can be reduced to those in the finite domain (integrals along the circle) for the circular function-based GKS. In addition, the Maxwellian distribution function can be reduced to a simple form, which only depends on macroscopic flow variables on the circle. These simplifications enable us to derive explicit formulations to compute macroscopic flow variables and numerical fluxes. As a consequence, the circular function-based GKS usually requires much less computational effort than the corresponding Maxwellian function-based GKS. On the other hand, as compared with the conventional Riemann solvers [29–31], the explicit formulations of circular function-based GKS for viscous flows are still complicated, which may not be easy for application by new users. So, practically, there is also a demand to replace the complicated formulations by a simple solution process. This motivates the present work.

Firstly, we use certain discrete points to represent the circle in the phase velocity space. Then, integrals along the circle for conservation forms of moments can be approximated by integral quadrature. The basic requirement is that the conservation forms of moments for the circular function-based GKS can be satisfied by weighted summation of distribution functions at discrete points. In fact, as shown in this paper, integral quadrature by four discrete points on the circle, which forms the D2Q4 discrete velocity model, can exactly match the integral. In this way, the macroscopic flow variables and numerical fluxes can be computed by weighted summations of distribution functions at discrete points, and the application of complicated formulations resulting from integrals is avoided. At the same time, since the equilibrium distribution function of circular function-based GKS is directly applied without any approximation, the method is still a kind of GKS. As such, like the Maxwellian function-based GKS, the present scheme can be applied to simulate flows from incompressible regime to hypersonic regime. To validate the present solver, some viscous incompressible and compressible flows are solved. Numerical results showed that for incompressible viscous flows, the computational accuracy of the present scheme is better than that of the standard lattice Boltzmann method (LBM) with D2Q9 model [32], and it agrees well with the circular function-based GKS [25]. In addition, for the compressible viscous flow, the computational efficiency of the present scheme is equivalent to that of the Roe scheme [33].

II. DEVELOPMENT OF DISCRETE VELOCITY MODELS FROM CIRCULAR FUNCTION-BASED GAS-KINETIC SCHEME (GKS)

A. Circular function-based GKS and seven conservation forms of moments

In this work, the discrete velocity models are developed from the circular function-based GKS, which was recently proposed by Shu and his co-workers [24,25]. As mentioned in the Introduction, the purpose of the developed discrete velocity model is to distribute discrete points on the circle in the phase velocity space so that the integrals in the circular function-based GKS can be simplified by weighted summation of distribution functions at discrete points. So, at the beginning, the circular function-based GKS and its seven conservation forms of moments are briefly introduced. The Boltzmann equation with Bhatnagar-Gross-Krook (BGK) collision model can be written as

$$\frac{\partial f}{\partial t} + \boldsymbol{\xi} \cdot \nabla f = \frac{g - f}{\tau}, \tag{1}$$

where f is the gas distribution function and g is the equilibrium state approached by f through particle collisions within a collision time scale τ. $\boldsymbol{\xi}$ is the particle velocity in the phase space. The equilibrium state is a Maxwellian distribution function. As reported in [24,25], for the two-dimensional case, the Maxwellian distribution function can be simplified to the circular function given by

$$g_C = \begin{cases} \frac{\rho}{2\pi} & \text{if} \quad (\xi_1 - u_1)^2 + (\xi_2 - u_2)^2 = c^2 \\ 0 & \text{otherwise} \end{cases}. \tag{2}$$

Here ρ is the density of mean flow; $\boldsymbol{\xi} = (\xi_1, \xi_2)$ and $\mathbf{u} = (u_1, u_2)$ are the phase velocity vector and the macroscopic flow velocity vector, respectively. The square of radius c actually represents the mean kinetic energy of the particles given by

$$c^2 = D(\gamma - 1)e, \tag{3}$$

where γ is the specific heat ratio, D is the abbreviation of the dimension ($D = 2$ for two dimensions). $e = p/[(\gamma - 1)\rho]$ is the potential energy of mean flow, where p is the pressure. The physical meaning of Eq. (2) is that all the mass, momentum, and energy are concentrated on the circle.

To construct the discrete velocity models from the circular function-based GKS, one of the fundamental requirements is that the developed models must satisfy the seven conservation forms of moments. From Eq. (2) and Fig. 1, the phase velocity components in the Cartesian coordinate system for the circular function-based GKS can be written as

$$\xi_1 = u_1 + c\cos(\theta), \tag{4a}$$

$$\xi_2 = u_2 + c\sin(\theta), \tag{4b}$$

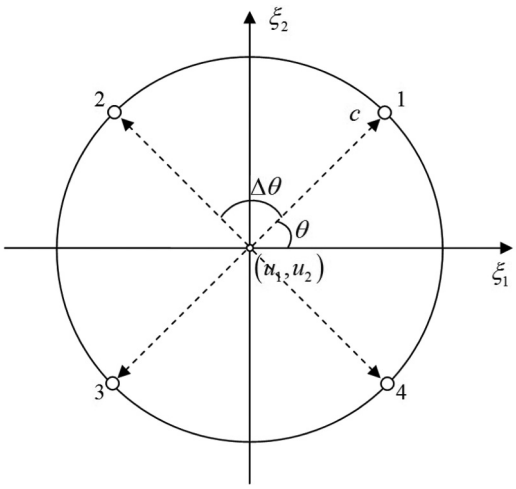

FIG. 1. Schematic diagram of D2Q4 model.

where θ is the angle between the radial direction and x direction, as shown in Fig. 1. With notations $c_1 = c\cos(\theta)$, $c_2 = c\sin(\theta)$, and $\xi_\alpha = u_\alpha + c_\alpha$, the seven conservation forms of moments for the circular function-based GKS, which are used to recover Navier-Stokes equations, can be expressed as [25,34]

$$\int_0^{2\pi} g_C d\theta = \rho, \tag{5a}$$

$$\int_0^{2\pi} g_C \xi_\alpha d\theta = \rho u_\alpha, \tag{5b}$$

$$\int_0^{2\pi} g_C(\xi_\alpha\xi_\alpha + 2e_p)d\theta = \rho(u_\alpha u_\alpha + bRT), \tag{5c}$$

$$\int_0^{2\pi} g_C \xi_\alpha\xi_\beta d\theta = \rho u_\alpha u_\beta + p\delta_{\alpha\beta}, \tag{5d}$$

$$\int_0^{2\pi} g_C\left(\xi_\alpha\xi_\alpha + 2e_p\right)\xi_\beta d\theta = \rho[u_\alpha u_\alpha + (b+2)RT]u_\beta, \tag{5e}$$

$$\int_0^{2\pi} g_C \xi_\alpha\xi_\beta\xi_\chi d\theta = p(u_\alpha\delta_{\beta\chi} + u_\beta\delta_{\chi\alpha} + u_\chi\delta_{\alpha\beta}) + \rho u_\alpha u_\beta u_\chi, \tag{5f}$$

$$\int_0^{2\pi} g_C(\xi_\chi\xi_\chi + 2e_p)\xi_\alpha\xi_\beta d\theta = \rho\{bR^2T^2\delta_{\alpha\beta} + [(b+4)u_\alpha u_\beta + u_\chi u_\chi\delta_{\alpha\beta}]RT + u_\chi u_\chi u_\alpha u_\beta\}, \tag{5g}$$

where ξ_α, ξ_β, ξ_χ and u_α, u_β, u_χ are the phase velocities and macroscopic flow velocities in the α, β, and χ direction, respectively. $e_p = [1 - D(\gamma-1)/2]e$ is the potential energy of particles. R is the gas constant and T is the temperature of mean flow. b is a constant related to γ; $b = 2/(\gamma-1)$. Equations (5a)–(5c) are used to recover the fluid density, momentum, and energy. Equations (5d) and (5e) are applied to recover convective fluxes of momentum equation and energy equation. Equations (5f) and (5g) are utilized to recover diffusive fluxes of momentum equation and energy equation. As pointed out in [25,34], the Prandtl number of the macroscopic governing equations recovered by the circular function-based GKS is fixed at γ. To consider the effect of Prandtl number, energy flux correction should be applied [25].

B. Basic requirement for development of discrete velocity models

Although the circular function-based GKS has been greatly simplified as compared with the Maxwellian function-based GKS, it is still a continuous model, and its explicit formulations for viscous flows [25] are still complicated. On the other hand, we notice that in the circular function-based GKS, only the particle velocities shown in Eq. (4) are related to the angle θ and the distribution function g_C shown in Eq. (2) is independent of θ. Obviously, when the particle velocity $\boldsymbol{\xi}$ and the distribution function g_C are substituted into Eq. (5), it only involves the integrals of sine and cosine functions of θ. To sum up, the seven forms of Eq. (5) involve the following integrals:

$$\int_0^{2\pi} \sin^{i-1}(\theta)\cos^{j-1}(\theta)d\theta = A_{ij}, \quad 1 \leqslant i+j \leqslant 5, \tag{6}$$

where A_{ij} is the result of the integral equation (6), and both i and j are the positive integers. For $1 \leqslant i+j \leqslant 5$, we have

$$A = \begin{bmatrix} 2\pi & 0 & \pi & 0 \\ 0 & 0 & 0 & \\ \pi & 0 & & \\ 0 & & & \end{bmatrix}. \tag{7}$$

To construct the discrete velocity models, Eq. (6) should be expressed as the form of integral quadrature, i.e.,

$$\sum_{m=1}^{M} \sin^{i-1}(\theta_m)\cos^{j-1}(\theta_m)\Delta\theta = A_{ij}, \quad 1 \leqslant i+j \leqslant 5, \tag{8}$$

where $\Delta\theta$ is the angle between two adjacent discrete points shown in Fig. 1; i.e., $\Delta\theta = 2\pi/M$. M is the number of the discrete points on the circle. θ_m is the angle of the mth discrete point, which can be computed by

$$\theta_m = \left(m - \frac{1}{2}\right)\Delta\theta, \quad m = 1,2,\ldots,M. \tag{9}$$

This reminds us that the discrete velocity models can be constructed by discretizing the angle θ into some discrete values as long as the relationship (8) can be exactly or accurately satisfied by the discrete angle, θ_m. Actually, Eq. (8) forms the framework of developing the discrete velocity models for simulation of viscous incompressible and compressible flows in this work.

C. D2Q4 and other discrete velocity models

Once the angle θ is discretized by Eq. (9), the corresponding discrete velocity model can be expressed as

$$g_m = \frac{\rho}{2\pi}, \quad m = 1,2,\cdots,M, \tag{10a}$$

$$\boldsymbol{\xi}_m = (\xi_{m,1},\xi_{m,2}) = [u_1 + c\cos(\theta_m), u_2 + c\sin(\theta_m)], \quad m = 1,2,\ldots,M. \tag{10b}$$

It should be pointed out that Eq. (10) is a general form of discrete velocity model, which may not satisfy Eq. (8). So, the question that remains is whether there is a value of M so that the developed discrete velocity model can exactly satisfy the relationship (8). To answer this question, let us set $M = 4K$, where K is a positive integer. For this case, we can have the following results:

$$\sum_{m=1}^{M} \sin^0(\theta_m)\cos^0(\theta_m)\Delta\theta = 2\pi, \quad \sum_{m=1}^{M} \sin^1(\theta_m)\cos^0(\theta_m)\Delta\theta = 0, \tag{11a}$$

$$\sum_{m=1}^{M} \sin^0(\theta_m)\cos^1(\theta_m)\Delta\theta = 0, \quad \sum_{m=1}^{M} \sin^2(\theta_m)\cos^0(\theta_m)\Delta\theta = \pi, \tag{11b}$$

$$\sum_{m=1}^{M} \sin^1(\theta_m)\cos^1(\theta_m)\Delta\theta = 0, \quad \sum_{m=1}^{M} \sin^0(\theta_m)\cos^2(\theta_m)\Delta\theta = \pi, \tag{11c}$$

$$\sum_{m=1}^{M} \sin^3(\theta_m)\cos^0(\theta_m)\Delta\theta = 0, \quad \sum_{m=1}^{M} \sin^2(\theta_m)\cos^1(\theta_m)\Delta\theta = 0, \tag{11d}$$

$$\sum_{m=1}^{M} \sin^1(\theta_m)\cos^2(\theta_m)\Delta\theta = 0, \quad \sum_{m=1}^{M} \sin^0(\theta_m)\cos^3(\theta_m)\Delta\theta = 0. \tag{11e}$$

Equation (11) shows that with $M = 4K$, the developed discrete velocity model can exactly satisfy the relationship (8). In other words, with $M = 4K$, the developed discrete velocity model can exactly satisfy the seven conservation forms of moments to recover Navier-Stokes equations. In this way, we do not need to use complicated formulations to compute flow variables and fluxes. Instead, we can simply use integral quadrature to compute them.

By choosing different values of K, different discrete velocity models can be developed. Specifically, we can take $K = 1$ to develop a four-points discrete velocity model. The schematic diagram of this model is shown in Fig. 1. The equilibrium distribution function and discrete velocities of this model are given by

$$g_m = \frac{\rho}{2\pi}, \quad m = 1,2,3,4, \tag{12a}$$

$$\boldsymbol{\xi}_m = \begin{cases} (u_1 + \sqrt{2}/2c, u_2 + \sqrt{2}/2c), & m = 1 \\ (u_1 - \sqrt{2}/2c, u_2 + \sqrt{2}/2c), & m = 2 \\ (u_1 - \sqrt{2}/2c, u_2 - \sqrt{2}/2c), & m = 3 \\ (u_1 + \sqrt{2}/2c, u_2 - \sqrt{2}/2c), & m = 4 \end{cases}. \tag{12b}$$

For simplicity, we name the four-points discrete velocity model as D2Q4 model in this work. Here, D denotes the dimension and Q represents the number of discrete velocities. Similarly, we can set $K = 2$ and $K = 3$ to develop the D2Q8 model and D2Q12 model, respectively. In this work, we mainly focus on the D2Q4 model to test its performances for simulation of viscous incompressible and compressible flows. At the same time, the D2Q8 and D2Q12 models are also used to test the influence of the number of discrete velocities on the computational accuracy and efficiency.

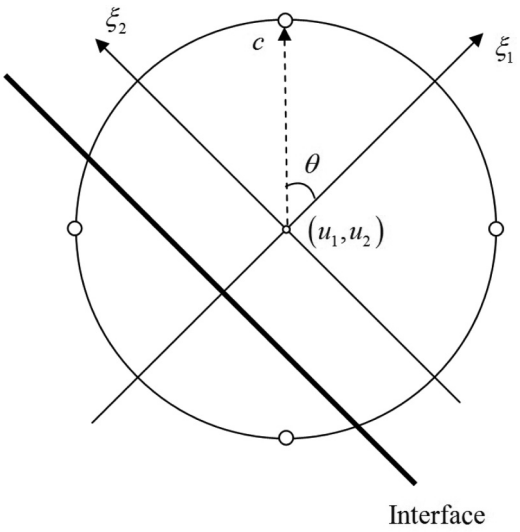

FIG. 2. Schematic diagram of discrete GKS with D2Q4 model.

III. DISCRETE GAS-KINETIC SCHEME FOR NAVIER-STOKES EQUATIONS

A. Navier-Stokes equations discretized by finite volume method

To apply the developed discrete GKS on arbitrary meshes, the finite volume method (FVM) is used to discretize the Navier-Stokes equations. For simplicity, the local coordinate system is utilized, which is defined in Fig. 2. In the local coordinate system, direction 1 is taken as the normal direction pointing outwards from the cell interface and direction 2 is chosen as the tangential direction of the cell interface. The discrete form of Navier-Stokes equations given by FVM can be written as

$$\frac{d\mathbf{W}_I}{dt} = -\frac{1}{\Omega_I}\sum_{i=1}^{N_f} \mathbf{F}_i S_i, \tag{13}$$

where I is the index of a control volume; Ω_I and N_f represent the volume and the number of interfaces of the control volume I, respectively. S_i denotes the area of the ith interface of the control volume. $\mathbf{W}$ and $\mathbf{F}$ are the vector of conservative variables at the cell center and flux vector at the cell interface, respectively. According to the conservation forms of moments (5), the connections between the distribution functions of the developed discrete velocity models f_m and the conservative variables $\mathbf{W}$ and flux vector $\mathbf{F}$ can be expressed as the following numerical integrations:

$$\mathbf{W} = (\rho, \rho u_1, \rho u_2, \rho E)^T = \sum_{m=1}^{M} \boldsymbol{\varphi}_m f_m \Delta\theta, \tag{14}$$

$$\mathbf{F} = (F_1, F_2, F_3, F_4)^T = \sum_{m=1}^{M} \xi_{m,1} \boldsymbol{\varphi}_m f_m \Delta\theta, \tag{15}$$

where E is the total energy of mean flow; $E = (u_1^2 + u_2^2)/2 + e$. $\boldsymbol{\varphi}_m$ stands for the moments

$$\boldsymbol{\varphi}_m = \left(1, \xi_{m,1}, \xi_{m,2}, \tfrac{1}{2}|\boldsymbol{\xi}_m|^2 + e_{p,m}\right)^T. \tag{16}$$

Note that in the current work, the conservative variables at the cell center $\mathbf{W}$ are not given from Eq. (14). Instead, they are obtained by marching Eq. (13) in time. As a consequence, the main task is to calculate the flux vector $\mathbf{F}$ at the cell interface.

In the practical calculation, we need to transform the flux vector $\mathbf{F}$ into the global coordinate system. In the global coordinate system, the flux vector is given by [25]

$$\mathbf{F}_n = (F_1, F_2 n_x - F_3 n_y, F_3 n_x + F_2 n_y, F_4)^T, \tag{17}$$

where $\mathbf{n} = (n_x, n_y)$ denotes the unit normal vector of the cell interface in the global coordinate system. It can be seen from Eq. (17) that the calculation of $\mathbf{F}_n$ is equivalent to evaluating $\mathbf{F}$ by Eq. (15) and the key issue is to obtain the discrete distribution functions f_m and the moments $\boldsymbol{\varphi}_m$.

B. Evaluation of numerical fluxes at cell interface

In this work, the developed D2Q4, D2Q8, and D2Q12 models are utilized to calculate the numerical fluxes by replacing the integral formulations of the circular function-based GKS with a simple solution process. Suppose that the cell interface is located at $\mathbf{r} = 0$. As shown in [25], the distribution function at the cell interface consists of an equilibrium part and a nonequilibrium part, which can be written as

$$\begin{aligned} f_m(0,t) &= f_m^{\mathrm{eq}}(0,t) + f_m^{\mathrm{neq}}(0,t) \\ &= g_m(0,t) + \tau_0[g_m(-\boldsymbol{\xi}_m \delta t, t - \delta t) \\ &\quad - g_m(0,t)] + O(\delta t^2), \end{aligned} \tag{18}$$

where $g_m(0,t) = f_m^{\mathrm{eq}}(0,t)$ is the equilibrium distribution function at the cell interface, and $g_m(-\boldsymbol{\xi}_m \delta t, t - \delta t)$ is the equilibrium distribution function on the circle. τ_0 is the dimensionless collision time, which can be calculated by

$$\tau_0 = \frac{\tau}{\delta t} = \frac{\mu}{p \delta t}, \tag{19}$$

where μ is the dynamic viscosity, which can be determined from Sutherland's law or the relationship of the Reynolds number. δt is the streaming time step, which will be discussed later. To simplify the notation, "$(0,t)$" is denoted by superscript "$face$" and "$(-\boldsymbol{\xi}_m \delta t, t - \delta t)$" is noted by superscript "cir" in the following text. Substituting Eq. (18) into Eq. (15), we can get

$$\begin{aligned} \mathbf{F} &= \sum_{m=1}^{M} \xi_{m,1}^{\mathrm{face}} \boldsymbol{\varphi}_m^{\mathrm{face}} g_m^{\mathrm{face}} \Delta\theta \\ &\quad + \tau_0 \left[\sum_{m=1}^{M} \xi_{m,1}^{\mathrm{cir}} \boldsymbol{\varphi}_m^{\mathrm{cir}} g_m^{\mathrm{cir}} \Delta\theta - \sum_{m=1}^{M} \xi_{m,1}^{\mathrm{face}} \boldsymbol{\varphi}_m^{\mathrm{face}} g_m^{\mathrm{face}} \Delta\theta \right] \\ &= \mathbf{F}^I + \tau_0[\mathbf{F}^{II} - \mathbf{F}^I]. \end{aligned} \tag{20}$$

From Eq. (20), it can be observed that there are two parts of flux at the cell interface. One is the flux attributed to the equilibrium distribution function and moments at the cell interface, which is denoted as $\mathbf{F}^I$. The other is the flux attributed to the equilibrium distribution function and moments on the circle, which is referred to as $\mathbf{F}^{II}$.

The schematic diagram of the current scheme is shown in Fig. 2. In order to calculate the fluxes $\mathbf{F}^I$ and $\mathbf{F}^{II}$, $\boldsymbol{\varphi}_m^{\mathrm{face}}$, g_m^{face}, $\boldsymbol{\varphi}_m^{\mathrm{cir}}$, and g_m^{cir} should be computed in advance. The moments and equilibrium distribution functions on the circle can be obtained from the conservative variables at the same physical positions. The conservative variables on the circle can be computed by

$$\mathbf{W}_m^{\mathrm{cir}} = \begin{cases} \mathbf{W}^L - \nabla \mathbf{W}^L \cdot \boldsymbol{\xi}_m^+ \delta t, & \text{if} \quad \xi_{m,1}^+ \geqslant 0 \\ \mathbf{W}^R - \nabla \mathbf{W}^R \cdot \boldsymbol{\xi}_m^+ \delta t, & \text{if} \quad \xi_{m,1}^+ < 0 \end{cases}, \tag{21}$$

where $\mathbf{W}^L$ and $\mathbf{W}^R$ are the conservative variables at the left and right side of the cell interface. $\nabla \mathbf{W}^L$ and $\nabla \mathbf{W}^R$ are the first-order derivatives of the conservative variables at the left and right cells around the cell interface, respectively. $\boldsymbol{\xi}_m^+$ is the predicted particle velocity at the cell interface given by

$$\boldsymbol{\xi}_m^+ = (\xi_{m,1}^+, \xi_{m,2}^+) = [u_1^+ + c^+ \cos(\theta_m), u_2^+ + c^+ \sin(\theta_m)]. \tag{22}$$

As mentioned in [25], the predicted mean flow velocities u_1^+ and u_2^+ and effective peculiar velocity c^+ can be given from those calculated in the previous time step. The details for calculation of these variables at the cell interface can be seen in Eqs. (25) and (26). At the beginning, the values of these variables can be simply given by the average of those at two sides of the cell interface. Once the conservative variables on the circle are obtained, the particle velocities, particle potential energy, and equilibrium distribution function can be calculated by

$$\xi_{m,1}^{\mathrm{cir}} = u_{m,1}^{\mathrm{cir}} + c^+ \cos(\theta_m), \tag{23a}$$

$$\xi_{m,2}^{\mathrm{cir}} = u_{m,2}^{\mathrm{cir}} + c^+ \sin(\theta_m), \tag{23b}$$

$$e_{p,m}^{\mathrm{cir}} = [1 - D(\gamma - 1)/2] e_m^{\mathrm{cir}}, \tag{23c}$$

$$g_m^{\mathrm{cir}} = \frac{\rho_m^{\mathrm{cir}}}{2\pi}, \tag{23d}$$

where ρ_m^{cir}, e_m^{cir}, $u_{m,1}^{\mathrm{cir}}$, and $u_{m,2}^{\mathrm{cir}}$ are the density, potential energy, normal velocity, and tangential velocity of mean flow on the circle, respectively. Substituting Eq. (23) into Eq. (15), we can obtain the numerical flux $\mathbf{F}^{II}$ as

$$\mathbf{F}^{II} = \begin{bmatrix} \sum_{m=1}^{M} \xi_{m,1}^{\mathrm{cir}} g_m^{\mathrm{cir}} \Delta\theta \\ \sum_{m=1}^{M} \xi_{m,1}^{\mathrm{cir}} \xi_{m,1}^{\mathrm{cir}} g_m^{\mathrm{cir}} \Delta\theta \\ \sum_{m=1}^{M} \xi_{m,1}^{\mathrm{cir}} \xi_{m,2}^{\mathrm{cir}} g_m^{\mathrm{cir}} \Delta\theta \\ \sum_{m=1}^{M} \xi_{m,1}^{\mathrm{cir}} \left(\frac{1}{2}|\boldsymbol{\xi}_m^{\mathrm{cir}}|^2 + e_{p,m}^{\mathrm{cir}}\right) g_m^{\mathrm{cir}} \Delta\theta \end{bmatrix}. \tag{24}$$

In order to calculate the flux attributed to $\boldsymbol{\varphi}_m^{\mathrm{face}}$ and g_m^{face}, the conservative variables at the cell interface should be computed first. As reported in [25], according to the compatibility condition, the conservative variables at the cell interface can be computed by

$$\mathbf{W}^{\mathrm{face}} = \sum_{m=1}^{M} \boldsymbol{\varphi}_m^{\mathrm{cir}} g_m^{\mathrm{cir}} \Delta\theta. \tag{25}$$

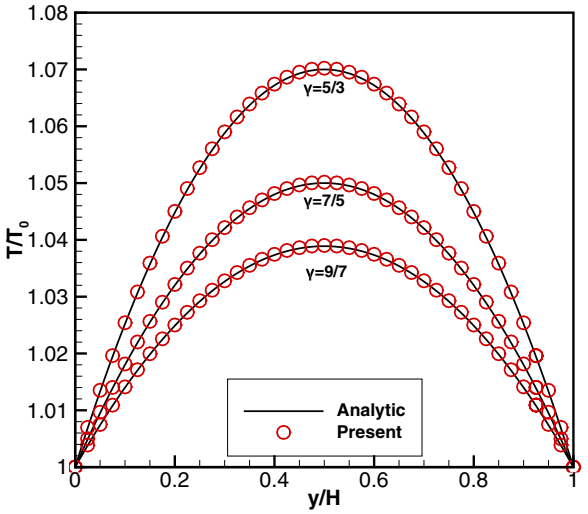

FIG. 3. Comparison of temperature profiles in steady Couette flow with different specific heat ratios.

Substituting Eq. (23) into Eq. (25), we can obtain the explicit expression of $\mathbf{W}^{\text{face}}$ as

$$\rho^{\text{face}} = \sum_{m=1}^{M} g_m^{\text{cir}} \Delta\theta, \tag{26a}$$

$$(\rho u_1)^{\text{face}} = \sum_{m=1}^{M} \xi_{m,1}^{\text{cir}} g_m^{\text{cir}} \Delta\theta, \tag{26b}$$

$$(\rho u_2)^{\text{face}} = \sum_{m=1}^{M} \xi_{m,2}^{\text{cir}} g_m^{\text{cir}} \Delta\theta, \tag{26c}$$

$$(\rho E)^{\text{face}} = \sum_{m=1}^{M} \left(\frac{1}{2} \left| \boldsymbol{\xi}_m^{\text{cir}} \right|^2 + e_{p,m}^{\text{cir}} \right) g_m^{\text{cir}} \Delta\theta. \tag{26d}$$

Once the conservative variables at the cell interface $\mathbf{W}^{\text{face}}$ are obtained, $\boldsymbol{\varphi}_m^{\text{face}}$ and g_m^{face} can be determined in a straightforward way, and the flux vector $\mathbf{F}^I$ can be evaluated by substituting $\boldsymbol{\varphi}_m^{\text{face}}$ and g_m^{face} into Eq. (15). An alternative but simpler way to compute $\mathbf{F}^I$ is to substitute the conservative variables $\mathbf{W}^{\text{face}}$ directly into the expression of inviscid flux, i.e.,

$$\mathbf{F}^I = \begin{bmatrix} \rho u_1 \\ \rho u_1 u_1 + p \\ \rho u_1 u_2 \\ (\rho E + p) u_1 \end{bmatrix}^{\text{face}}. \tag{27}$$

Substituting Eqs. (24) and (27) into Eq. (20), we can obtain the whole expression of the numerical fluxes for Navier-Stokes equations.

The last undetermined variable in Eq. (20) is the streaming time step δt. Note that δt is not the real time step to march in time. It is only used at the cell interface to reconstruct the local solution and is related to the collision time τ_0 by Eq. (19). The

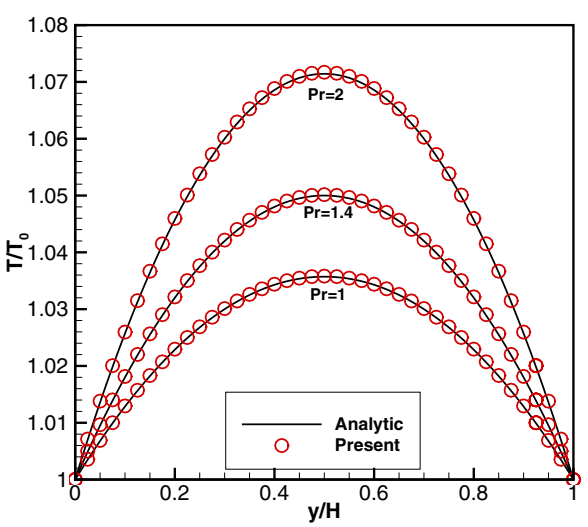

FIG. 4. Comparison of temperature profiles in steady Couette flow with different Prandtl numbers.

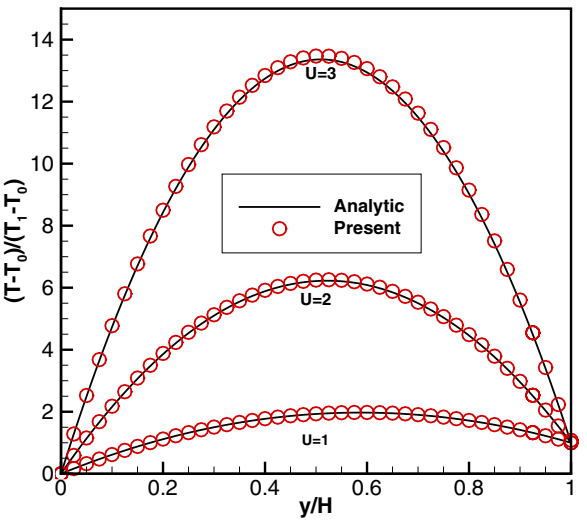

FIG. 5. Comparison of temperature profiles in steady Couette flow with different moving velocities at top plate.

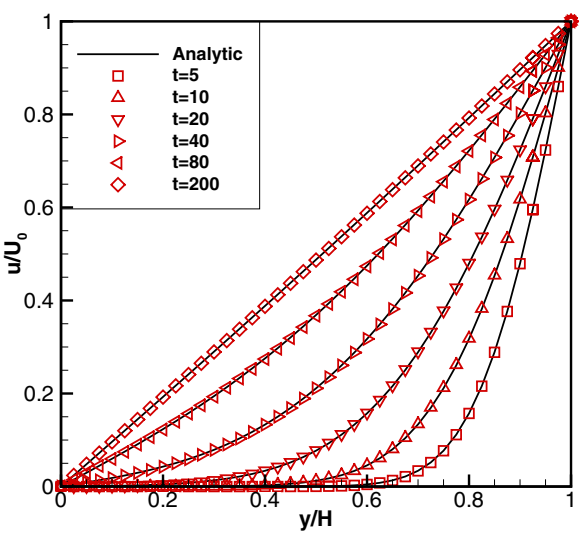

FIG. 6. Comparison of u-velocity profiles in unsteady Couette flow at various simulation times.

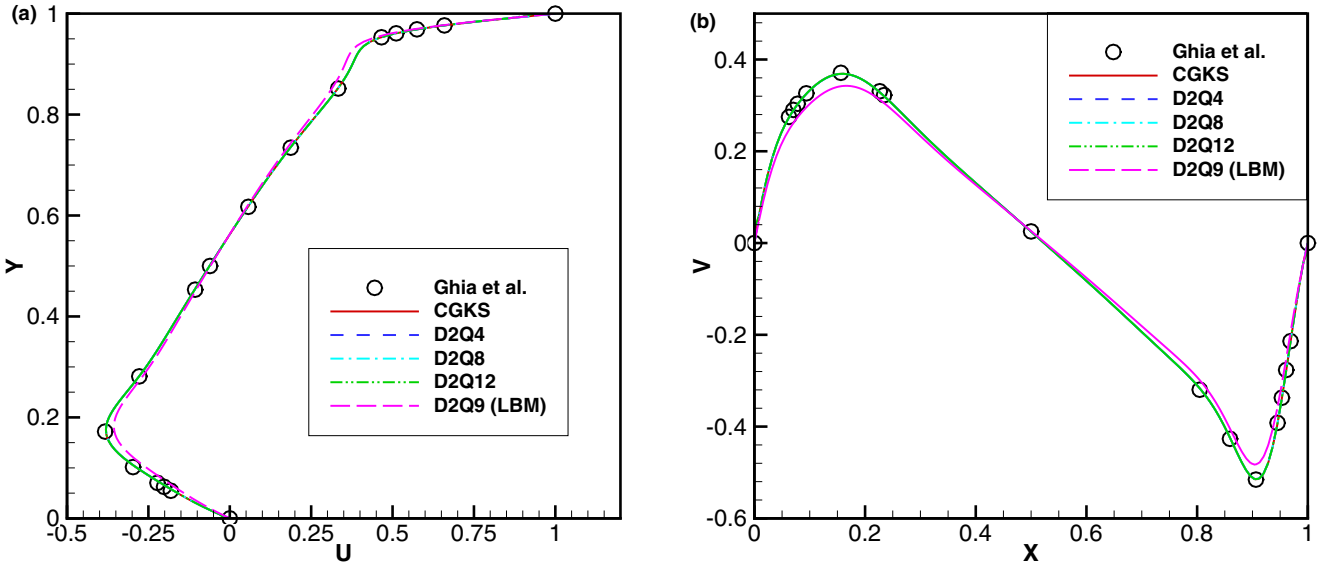

FIG. 7. Comparison of velocity profiles for lid-driven cavity flows at Re = 1000. (a) u-velocity profiles along vertical central line. (b) v-velocity profiles along horizontal central line.

principle for the choice of δt is that the circle in the physical space must be within the cell of the interface in order to avoid extrapolation. In this work, δt is determined by

$$\delta t = \frac{0.2\min\{\Delta l, \Delta r\}}{(\max\{u_1^+, u_2^+\} + c^+)}, \tag{28}$$

where Δl and Δr are the shortest edge of the left and right cells around the cell interface, respectively. In this way, the extrapolation is avoided for any nonexcessive distorted structured and unstructured meshes.

In addition, as mentioned in Sec. II A, the Prandtl number of the macroscopic governing equations recovered by the circular function-based GKS is fixed at γ. In order to solve problems with different Prandtl number, a convenient approach is to make a correction for energy flux. The heat flux can be expressed as

$$q = -k\nabla T \cdot \mathbf{n} = -\frac{\gamma\mu}{(\gamma - 1)\,\mathrm{Pr}}\nabla T \cdot \mathbf{n}, \tag{29}$$

where k is the thermal conductivity and Pr is the Prandtl number. The gradient of temperature at the cell interface takes the mean value of those from the cells around the cell interface. With Eq. (29), the correct energy flux is calculated by

$$F_4^{\mathrm{correct}} = F_4 + \left(1 - \frac{\mathrm{Pr}}{\gamma}\right)q. \tag{30}$$

It is found that the above remedy is quite simple and effective with very little increment of computational effort.

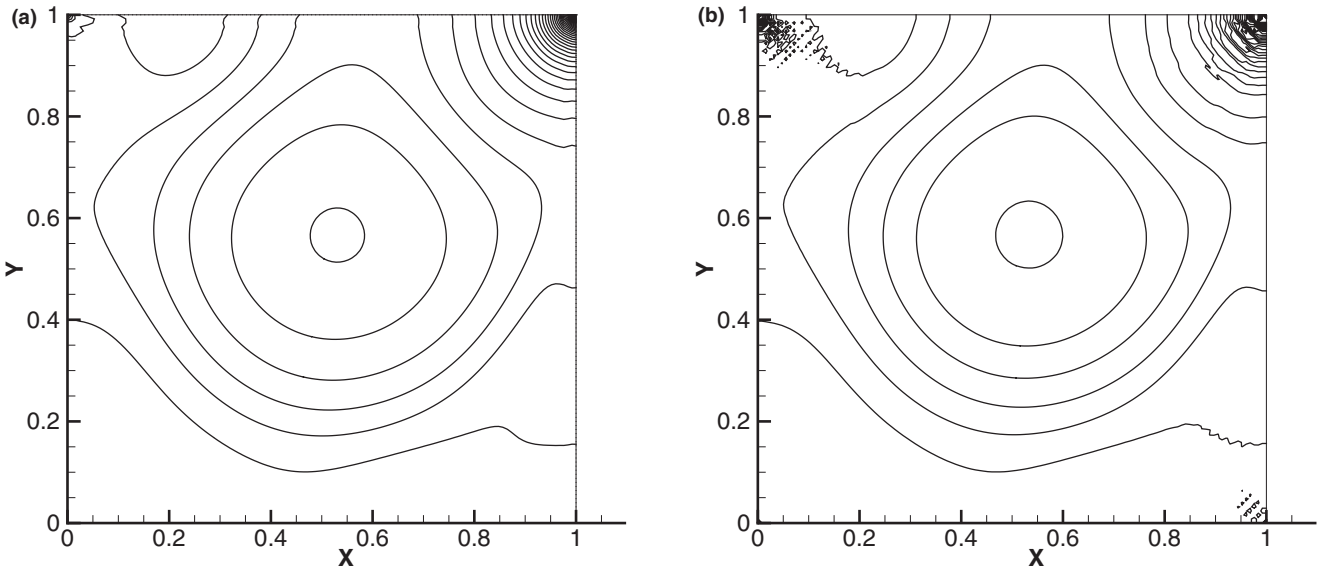

FIG. 8. Comparison of pressure contours for lid-driven cavity flows at Re = 1000. (a) Results of present scheme with D2Q4 model. (b) Results of standard LBM with D2Q9 model.

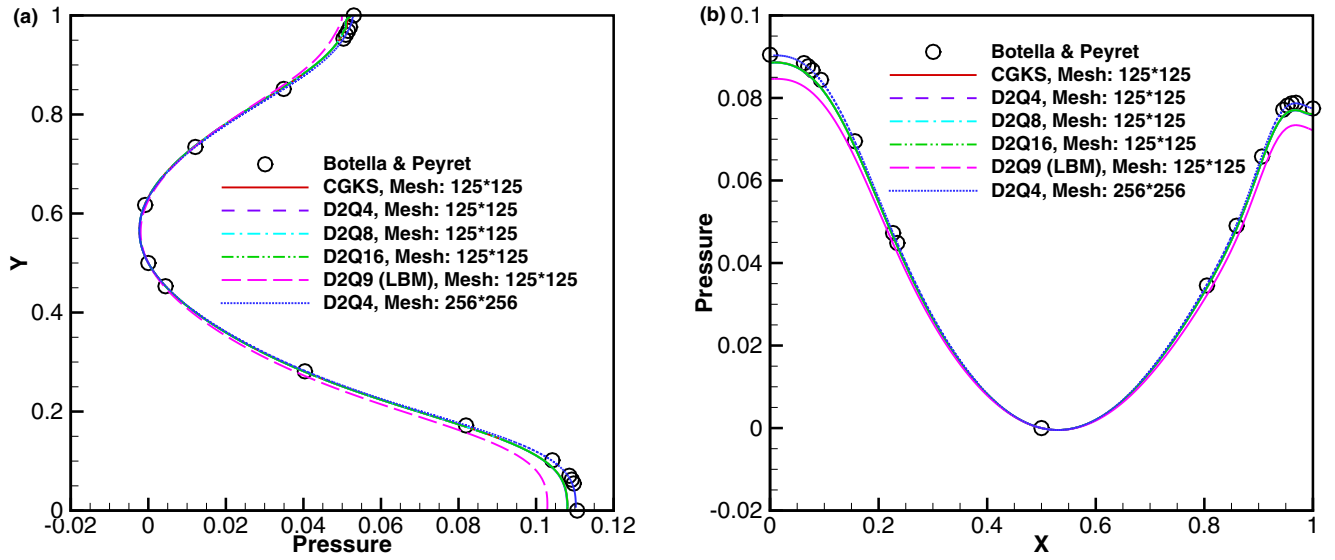

FIG. 9. Comparison of pressure profiles for lid-driven cavity flows at Re = 1000. (a) Pressure profiles along vertical central line. (b) Pressure profiles along horizontal central line.

C. Basic computational sequence

The basic solution procedure of the present scheme is outlined below:

(1) Calculate the derivatives of conservative variables and reconstruct the initial conservative variables at two sides of the cell interface.

(2) Assign the values of u_1^+, u_2^+, and c^+ at the cell interface from those in the previous time step, and further compute the predicted particle velocity $\boldsymbol{\xi}_m^+$ with Eq. (22).

(3) Compute the streaming time step δt by using Eq. (28) and the dimensionless collision time τ_0 with Eq. (19).

(4) Use Eq. (21) to calculate the conservative variables at the discrete points on the circle $\mathbf{W}_m^{\text{cir}}$, and further compute the particle velocities, particle potential energy, and equilibrium distribution function with Eq. (23).

(5) Calculate the flux $\mathbf{F}^{II}$ by using Eq. (24) and the conservative variables at the cell interface $\mathbf{W}^{\text{face}}$ with Eqs. (25) and (26), and further compute the flux $\mathbf{F}^{I}$ with Eq. (27).

(6) Compute the total flux across the cell interface $\mathbf{F}$ by using Eq. (20), and further convert $\mathbf{F}$ from the local coordinate system to the global coordinate system with Eq. (17).

(7) Use Eq. (29) to calculate the heat flux q, and make correction for F_4^{correct} with Eq. (30).

(8) Solve Eq. (13) in the global coordinate system by using the three-stage Runge-Kutta method. This step gives the conservative variables at the cell centers at the new time step.

(9) Repeat steps (1)–(8) until the converged solution is reached.

TABLE I. Comparison of computational effort for different discrete velocity models.

Discrete velocity models	Computational effort
D2Q4	1
D2Q8	1.539
D2Q12	1.820

Note: The computational effort of the D2Q8 and D2Q12 models is normalized by that of the D2Q4 model.

IV. NUMERICAL EXAMPLES

To validate the present scheme, several viscous incompressible and compressible flows are simulated. In the simulation, the conservative variables at two sides of the cell interface are interpolated from those at the cell centers and the Venkatakrishnan limiter [35] is used. For temporal discretization of Eq. (13), the three-stage Runge-Kutta method is applied. Unless otherwise stated, in all numerical examples reported in this work, the Courant-Friedrichs-Lewy (CFL) number is set as 1, the specific heat ratio is chosen as 1.4, and the Prandtl number is taken as 0.72. In addition, all the computations were done on a PC with 3.2 GHz CPU.

A. Case 1: Couette flow

The first test case is the Couette flow, which is used to validate the present D2Q4 model for different specific heat ratios, Prandtl numbers, and Mach numbers. This problem can be considered as a viscous fluid flow between two infinite parallel plates separated by a distance of H. The bottom plate is stationary and the top one is moving at a speed U in the horizontal direction. The temperature at the bottom and top walls is fixed as T_0 and T_1, respectively. In a steady state, under the assumption of constant viscosity and heat conduction coefficient, the temperature profiles can be obtained as [36]

$$T - T_0 = \Pr \frac{U^2}{2c_p} \frac{y}{H}\left(1 - \frac{y}{H}\right), \quad \text{when} \quad T_0 = T_1, \tag{31}$$

$$\frac{T - T_0}{T_1 - T_0} = \frac{y}{H} + \Pr \frac{\text{Ec}}{2} \frac{y}{H}\left(1 - \frac{y}{H}\right), \quad \text{when} \quad T_0 \neq T_1, \tag{32}$$

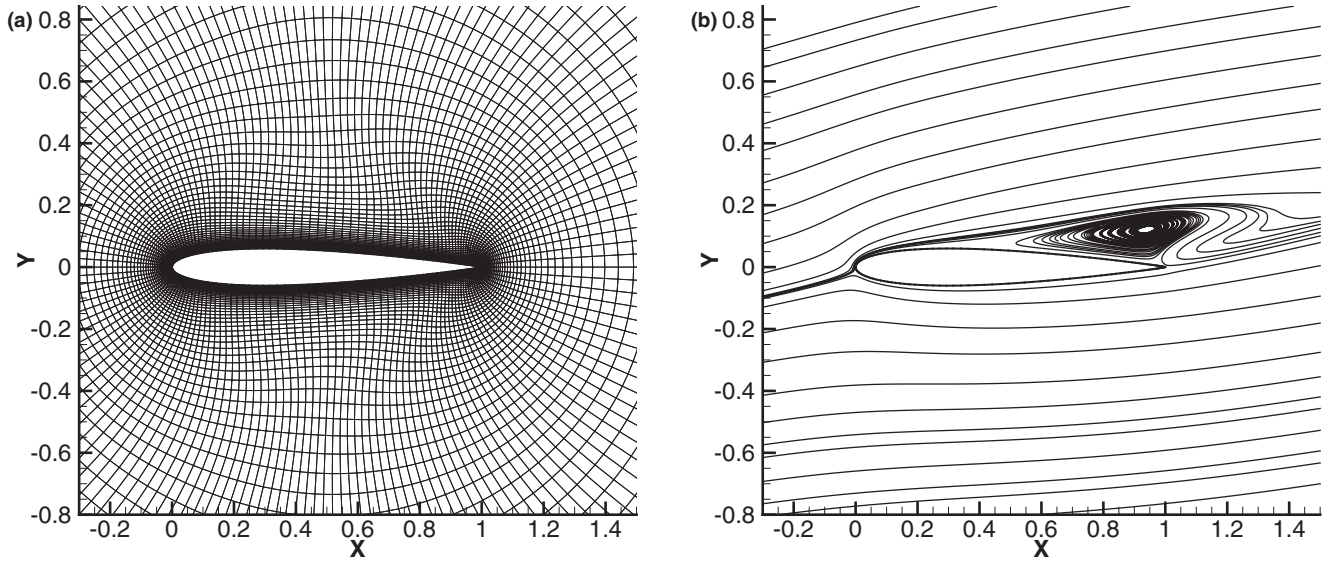

FIG. 10. (a) Partial view of computational mesh for NACA0012 airfoil. (b) Streamline pattern for transonic flow around NACA0012 airfoil.

where y is the distance from the bottom boundary, c_p is the specific heat ratio at constant pressure, and $\mathrm{Ec} = U^2/c_p(T_1 - T_0)$ is the Eckert number. If the flow velocity is initialized to zero, the velocity profile in the horizontal direction for $T_0 = T_1$ at various instants can be expressed as [36]

$$\frac{u_x}{U} = \frac{y}{H} + \frac{2}{\pi}\sum_{n=1}^{\infty}\left[\frac{(-1)^n}{n}\exp\left(-n^2\pi^2\frac{\mu t}{\rho H^2}\right)\sin\left(\frac{n\pi y}{H}\right)\right]. \tag{33}$$

In this case, we set the distance of two plates as $H = 1$ and a uniform mesh with 10×40 cells is used. At the inlet and outlet, a periodic boundary condition is implemented.

At first, the test case with different specific heat ratios, $\gamma = 5/3$, $7/5$, and $9/7$, and $\mathrm{Pr} = 1.4$, $U = u_0$, $T_1 = T_0$, is simulated. The temperature profiles obtained by the D2Q4 model along the vertical central line are compared with the analytic results in Fig. 3. It is observed that all the results of the present scheme exactly agree with the analytic data. Secondly, the test case with different Prandtl numbers of $\mathrm{Pr} = 1$, 1.4, and 2, and $\gamma = 7/5$, $U = u_0$, $T_1 = T_0$, is solved. As shown in Fig. 4, the results of the D2Q4 model for these cases also agree fairly well with the analytic solutions. Thirdly, the test case with different top plate velocities, $U = u_0$, $2u_0$, and $3u_0$, and $\gamma = 7/5$, $\mathrm{Pr} = 2$, $T_1 = (1 + 0.5)T_0$, is simulated. According to the definition of the Mach number, $\mathrm{Ma} = U/\sqrt{\gamma p/\rho}$, the Mach number of these test cases corresponds to 0.845, 1.690, and 2.535, respectively. Figure 5 shows that the present results match very well with the analytic ones, even when the flow is supersonic. Finally, we simulate the test case with

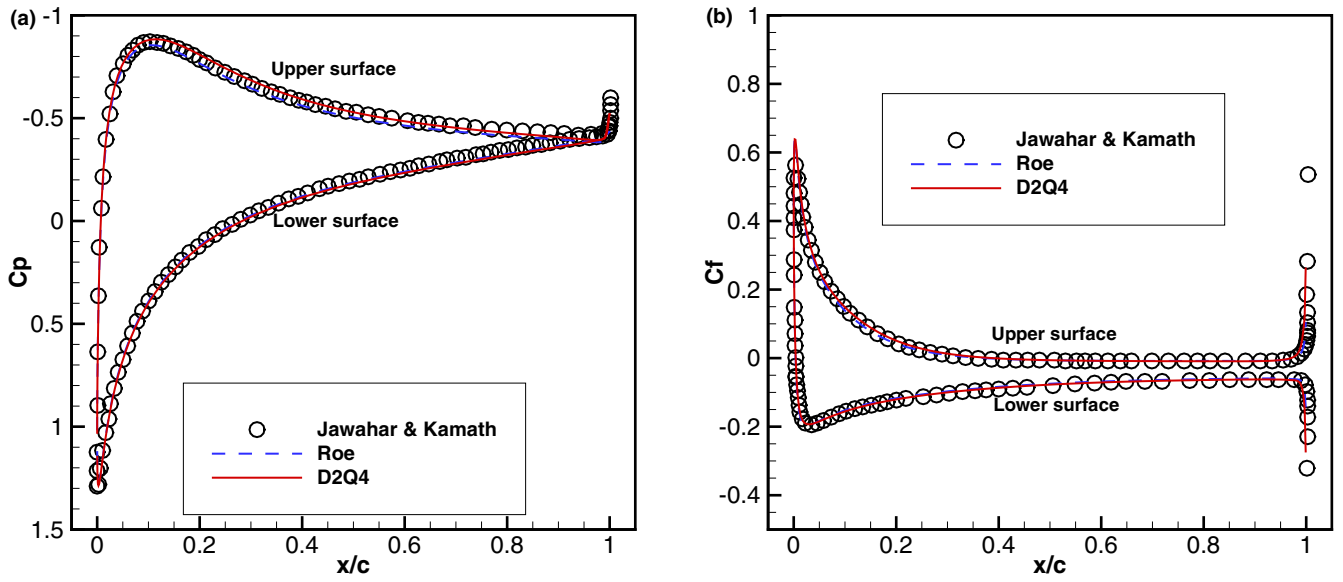

FIG. 11. (a) Comparison of pressure coefficient distribution for NACA0012 airfoil. (b) Comparison of skin friction coefficient distribution for NACA0012 airfoil.

TABLE II. Comparison of lift and drag coefficients for NACA0012 case.

References	C_{d_p}	C_{d_f}	$C_{d_{\text{total}}}$	$C_{l_{\text{total}}}$
GAMM [41]			0.243–0.2868	0.4145–0.517
Jawahar and Kamath [39]	0.152 87	0.124 39	0.277 26	0.502 31
Roe	0.149 05	0.126 68	0.275 73	0.444 68
D2Q4	0.154 77	0.131 10	0.285 87	0.474 49

Note: C_{d_p}, C_{d_f}, $C_{d_{\text{total}}}$, and $C_{l_{\text{total}}}$ are the pressure drag coefficient, friction drag coefficient, total drag coefficient, and total lift coefficient, respectively.

$\gamma = 7/5, \text{Pr} = 2, U = u_0$, and $T_1 = T_0$ to compare the velocity profiles at various instants. As shown in Fig. 6, the results obtained by the present scheme are in excellent agreement with the analytic data. This demonstrates that the effect of Prandtl number and specific heat ratio can be well considered in the present scheme.

B. Case 2: Lid-driven cavity flow

The second test case is the lid-driven cavity flow, in which the Mach number is set as 0.15. Thus this test case can be viewed as the incompressible fluid flow problem. For this test example, the velocity of the lid is taken as $U = 1$, the initial density of the fluid is set as $\rho = 1$, the cavity length-based Reynolds number is chosen as 1000, and the dynamic viscosity μ is determined from $\text{Re} = \rho U L/\mu$. In the simulation, the square domain with length $L = 1$ is divided uniformly into 125×125 cells. Figure 7 shows the comparison of u-velocity and v-velocity profiles along vertical and horizontal central lines obtained by the present scheme with the D2Q4, D2Q8, and D2Q12 models. Also displayed in this figure are the results of Ghia *et al.* [37], which are obtained by solving the incompressible Navier-Stokes equations, and the results obtained by using the circular function-based GKS [25] and the standard LBM with the D2Q9 model [32]. As shown in this figure, the results of the present scheme with the D2Q4, D2Q8, and D2Q12 models and circular function-based GKS are close to each other, and they accurately agree with the benchmark data [37]. However, by using the same grid, the standard LBM with the D2Q9 model provides a poorer result with large dissipation. Figure 8 compares the pressure contours obtained from the present scheme with the D2Q4 model and the standard LBM with the D2Q9 model. It is obvious that the results of LBM for the pressure field have substantial unphysical oscillations at the top left and top right corners while those of the present scheme are smooth all over the flow domain. The comparison of pressure profiles along the vertical and horizontal central lines are shown in Fig. 9. It can be seen that the results of the present scheme with the D2Q4, D2Q8, and D2Q12 models also match very well with those of circular function-based GKS, but all of them deviate slightly from the results of Botella and Peyret [38] in the vicinity of wall boundaries. In the meanwhile, obvious disparity between the results of LBM and those of Botella and Peyret [38] can be clearly observed near the wall boundaries. If the computational mesh is refined uniformly to 256×256 cells, both the results of the present scheme and circular function-based GKS compare well with those of Botella and Peyret [38]. To make the figure concisely, only the results of the D2Q4 model with refined mesh are shown in Fig. 9. In addition, the comparison of computational effort required by three discrete velocity models is made in Table I. It can be seen that the computational

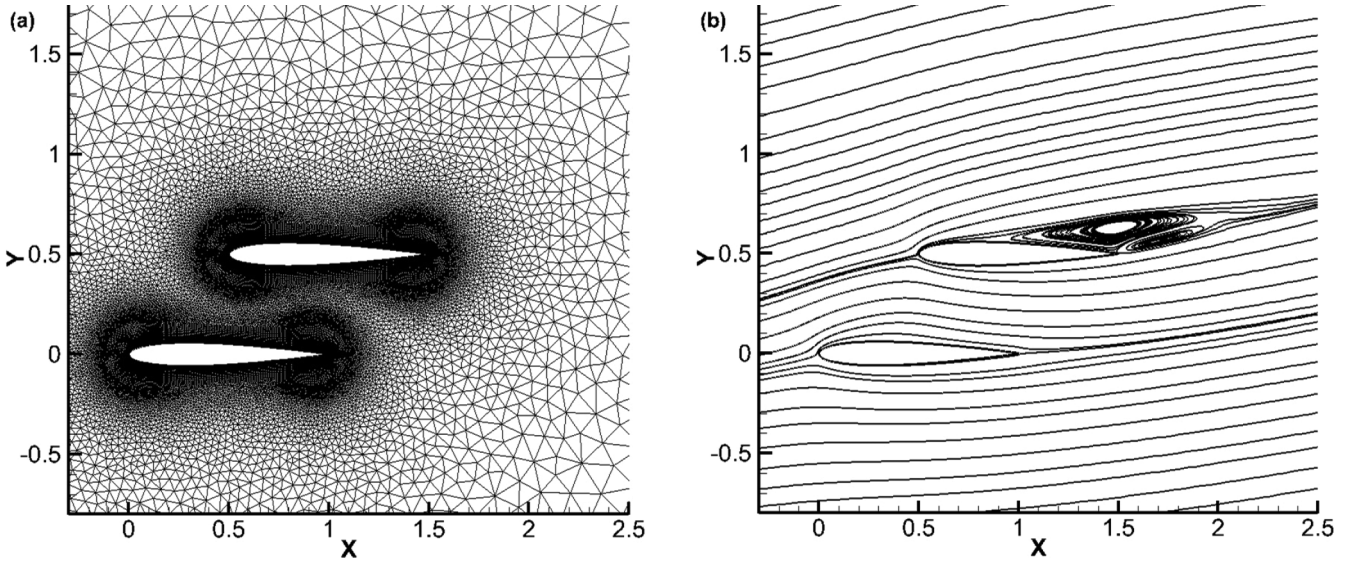

FIG. 12. (a) Partial view of computational mesh for biplane configuration. (b) Streamline pattern for transonic flow around biplane configuration.

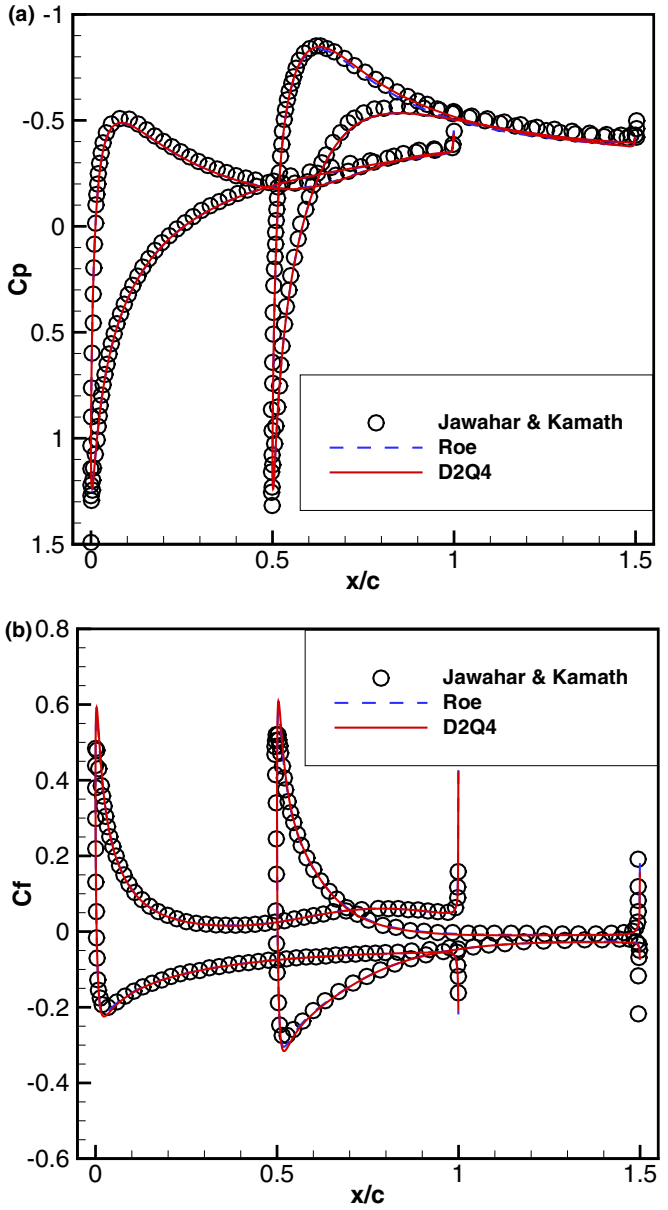

FIG. 13. (a) Comparison of pressure coefficient distribution for biplane configuration. (b) Comparison of skin friction coefficient distribution for biplane configuration.

efficiency of the D2Q4 model is inherently better than those of the D2Q8 and D2Q12 models. This test example shows that the accuracy of the present scheme is better than that of the standard LBM with D2Q9 model, and it is not affected by the number of discrete velocities. As a consequence, in the following test cases, only the D2Q4 model is applied.

TABLE III. Comparison of computational effort for different numerical schemes.

Schemes	NACA0012 airfoil	Biplane configuration
Roe	1	1
D2Q4	1.105	1.029

Note: The computational effort of the D2Q4 model is normalized by that of the Roe scheme.

C. Case 3: Transonic flow around NACA0012 airfoil and biplane configuration

To validate the present scheme for simulation of flows with complex geometry, the transonic flows around one NACA0012 airfoil and a staggered-biplane configuration are simulated. This test example is taken from the work of Jawahar and Kamath [39]. For all the simulations of this test case, the free-stream Mach number is 0.8, the chord length-based Reynolds number is 500, and the angle of attack is 10°.

At first, the test case of one NACA0012 airfoil is considered. In the test, the O-type grid with 160 points on the airfoil and 70 points in the radial direction is utilized, and its partial view is shown in Fig. 10(a). The computational domain is about ten times the chord length. Figure 10(b) shows the streamline pattern obtained by the D2Q4 model. It can be observed that the main feature of the flow, a prominent vortex that extends over 50% of the chord on the upper surface as captured by the D2Q4 model, compares well with that reported in [39,40]. The comparison of pressure coefficient and skin friction coefficient distributions on the airfoil surface obtained by the D2Q4 model and the Roe scheme [33] are respectively shown in Figs. 11(a) and 11(b). Also presented in the figures

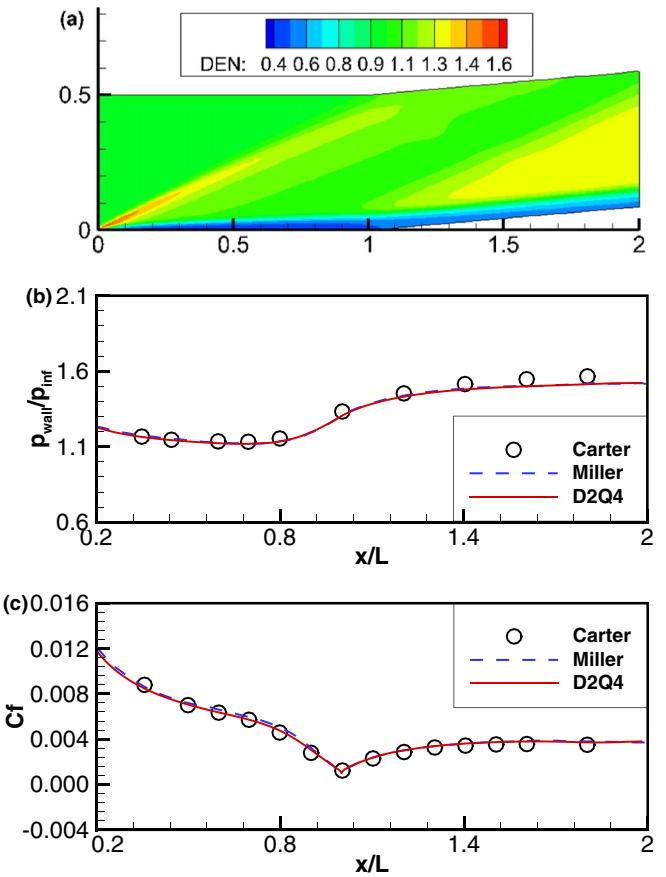

FIG. 14. Simulation results for supersonic flow around a 5° ramp. (a) Density contours. (b) Wall pressure distribution. (c) Skin friction distribution.

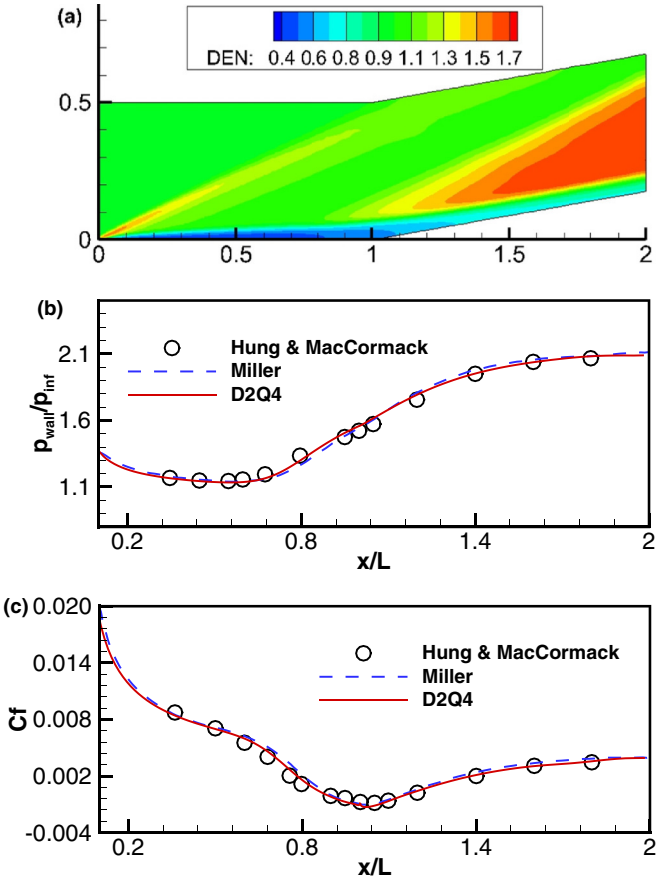

FIG. 15. Simulation results for supersonic flow around a 10° ramp. (a) Density contours. (b) Wall pressure distribution. (c) Skin friction distribution.

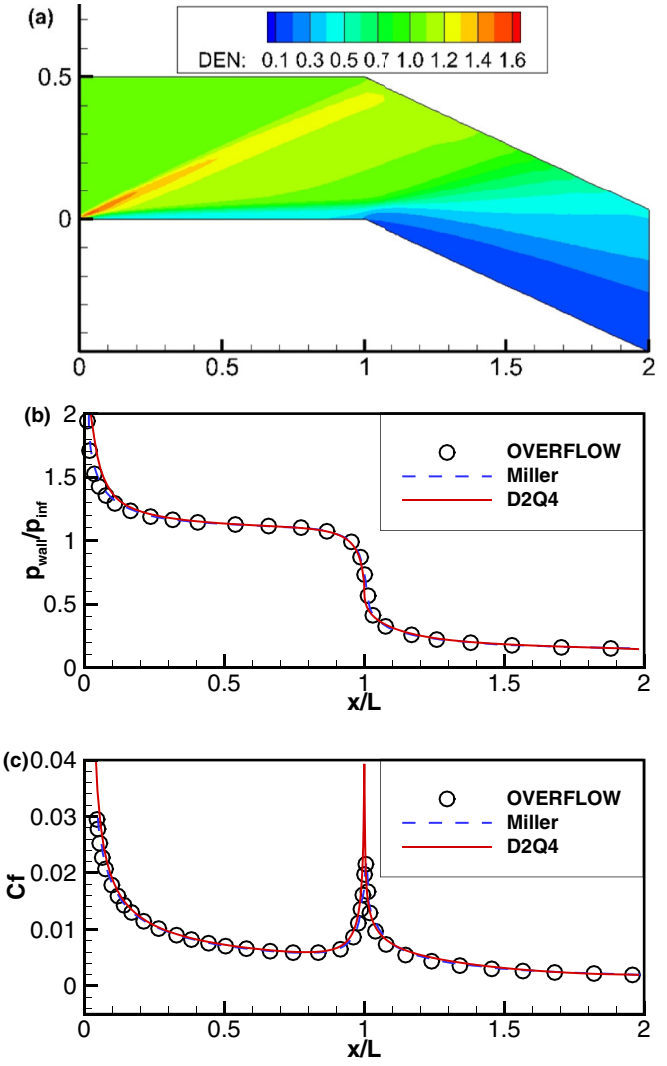

FIG. 16. Simulation results for supersonic flow around a −25° ramp. (a) Density contours. (b) Wall pressure distribution. (c) Skin friction distribution.

are the results of Jawahar and Kamath [39]. As can be seen from these figures, the results of the D2Q4 model and the Roe scheme are close to each other, and they basically agree well with the published data. In the meantime, the lift and drag coefficients obtained by the D2Q4 model and the Roe scheme are compared in Table II with the reference data of Gesellschaft für Angewandte Mathematik und Mechanik (GAMM) [41] and Jawahar and Kamath [39]. The results of the D2Q4 model are close to those of the Roe scheme and Jawahar and Kamath [39] and are well within the range reported in the GAMM workshop.

In addition, we consider the test case of a staggered NACA0012 biplane configuration. This test case comprises two NACA0012 airfoils, staggered by half a chord length in the pitchwise as well as chordwise directions. In the test, the unstructured grid containing 320 points on each airfoil with 54 387 triangular cells in the computational domain is utilized, and its partial view is shown in Fig. 12(a). The streamline pattern obtained by the present scheme with the D2Q4 model is shown in Fig. 12(b). By comparing Figs. 12(b) and 10(b), it can be found that the separation region on the upper surface of the top airfoil reveals two vortices in the test case of biplane configuration. The secondary vortex is introduced apparently by the bottom airfoil. This observation is in line with the results reported in [39]. Figures 13(a) and 13(b) respectively show the comparison of pressure coefficient and skin friction coefficient distributions on the airfoil surface. Once again, the results obtained by the D2Q4 model and the Roe scheme are close to each other, and they compare well with the results of Jawahar and Kamath [39]. In addition, as reported in Table III, the computational effort of the D2Q4 model is almost the same as that of the Roe scheme as the number of computational mesh increases. This test example demonstrates that the present scheme can well simulate viscous compressible flows on arbitrary meshes with roughly the same computational cost as that required by the commonly used Roe scheme [33].

D. Case 4: Supersonic flow around a ramp segment

Supersonic and hypersonic fluid flow problems have been widely studied both experimentally [42,43] and numerically [44–46]. In the last test case, the supersonic flow around a ramp segment with 5°, 10°, and -25° is considered. For this test case, the free-stream Mach number is 3.0, the Reynolds number based on the length of the flat region is 1.68×10^4, the

free-stream temperature is 216.7 K, and the wall temperature is fixed as 606.7 K. Both the length of the flat region and the ramp segment are taken as 1 m. The distance between the upper boundary of the computational domain and the bottom wall is fixed as 0.5 m. In the simulation, the nonuniform mesh with 240 × 70 cells is utilized. In addition, the CFL number is chosen as 0.5 to avoid divergence.

Figures 14–16 show the simulation results for the supersonic flow around a ramp segment with 5°, 10°, and -25°, respectively. From the figure of skin friction distribution, it can be found that only in the test case of the ramp angle of 10° does a separated flow region appear near the corner. For the test cases of the ramp angle of 5° and -25°, there is no separated flow region observed, but the ramp induces significant upstream effects. These observations are consistent with the results of Miller [44]. Also displayed in the figures are the results of Carter [45], Miller [44], Hung and MacCormack [46], and OVERFLOW provided by Miller [44]. Clearly, the results of the present scheme compare well with the published data. This test example well shows the capability of the present scheme for simulation of supersonic flows.

V. CONCLUSIONS

In this work, a platform for developing discrete velocity models is presented from the circular function-based gas-kinetic scheme (GKS). Based on the platform, the D2Q4, D2Q8, and D2Q12 models can be easily constructed for simulation of viscous incompressible and compressible flows. By using the proposed models, the complicated formulations of circular function-based GKS for viscous flows can be replaced by a simple solution process. In addition, due to the use of FVM, the present scheme is capable for simulation of flows with complex geometry. Numerical experiments, including the Couette flow, lid-driven cavity flow, transonic flow around NACA0012 airfoil and biplane configuration, and supersonic flow around a ramp segment, show that the viscous incompressible and compressible flows can be well simulated by the present scheme. It was also found that the number of discrete velocities in the phase velocity space has no effect on the accuracy of numerical results. Moreover, the computational efficiency of the D2Q4 model is roughly the same as that of the conventional Navier-Stokes solver [33].

[1] Z. Guo, H. Liu, L. S. Luo, and K. Xu, A comparative study of the LBE and GKS methods for 2D near incompressible laminar flows, J. Comput. Phys. **227**, 4955 (2008).

[2] S. Chen, C. Jin, C. Li, and Q Cai, Gas-kinetic scheme with discontinuous derivative for low speed flow computation, J. Comput. Phys. **230**, 2045 (2011).

[3] R. Yuan, C. Zhong, and H. Zhang, An immersed-boundary method based on the gas kinetic BGK scheme for incompressible viscous flow, J. Comput. Phys. **296**, 184 (2015).

[4] H. Z. Tang, Gas-kinetic schemes for compressible flow of real gases, Comput. Math. Appl. **41**, 723 (2001).

[5] A. A. Omar, O. J. Chit, L. J. Hsuh, and W. Asrar, Finite difference gas-kinetic BGK scheme for compressible inviscid flow computation, Int. J. Comput. Fluid Dyn. **22**, 183 (2008).

[6] J. Li, Q. Li, and K. Xu, Comparison of the generalized Riemann solver and the gas-kinetic scheme for inviscid compressible flow simulations, J. Comput. Phys. **230**, 5080 (2011).

[7] L. Tang, Progress in gas-kinetic upwind schemes for the solution of Euler/Navier-Stokes equations—I: Overview, Comput. Fluids **56**, 39 (2012).

[8] K. Xu and J. C. Huang, A unified gas-kinetic scheme for continuum and rarefied flows, J. Comput. Phys. **229**, 7747 (2010).

[9] S. Chen, K. Xu, C. Lee, and Q. Cai, A unified gas kinetic scheme with moving mesh and velocity space adaptation, J. Comput. Phys. **231**, 6643 (2012).

[10] J. C. Huang, K. Xu, and P. Yu, A unified gas-kinetic scheme for continuum and rarefied flows II: Multi-dimensional cases, Commun. Comput. Phys. **12**, 662 (2012).

[11] S. Xiong, C. Zhong, C. Zhuo, K. Li, X. Chen, and J. Cao, Numerical simulation of compressible turbulent flow via improved gas-kinetic BGK scheme, Int. J. Numer. Methods Fluids **67**, 1833 (2011).

[12] G. Kumar, S. S. Girimaji, and J. Kerimo, WENO-enhanced gas-kinetic scheme for direct simulations of compressible transition and turbulence, J. Comput. Phys. **234**, 499 (2013).

[13] K. Xu, M. Mao, and L. Tang, A multidimensional gas-kinetic BGK scheme for hypersonic viscous flow, J. Comput. Phys. **203**, 405 (2005).

[14] L. M. Yang, C. Shu, and J. Wu, A three-dimensional explicit sphere function-based gas-kinetic flux solver for simulation of inviscid compressible flows, J. Comput. Phys. **295**, 322 (2015).

[15] D. I. Pullin, Direct simulation methods for compressible inviscid ideal-gas flow, J. Comput. Phys. **34**, 231 (1980).

[16] J. C. Mandal and S. M. Deshpande, Kinetic flux vector splitting for Euler equations, Comput. Fluids **23**, 447 (1994).

[17] S.Y. Chou and D. Baganoff, Kinetic flux-vector splitting for the Navier-Stokes equations, J. Comput. Phys. **130**, 217 (1997).

[18] J. Y. Yang, T. Y. Hsieh, Y. H. Shi, and K. Xu, High-order kinetic flux vector splitting schemes in general coordinates for ideal quantum gas dynamics, J. Comput. Phys. **227**, 967 (2007).

[19] K. Xu, Gas-kinetic schemes for unsteady compressible flow simulations, Lect. Ser. - von Kareman Inst. Fluid Dyn. **3**, C1 (1998).

[20] K. Xu, A gas-kinetic BGK scheme for the Navier-Stokes equations and its connection with artificial dissipation and Godunov method, J. Comput. Phys. **171**, 289 (2001).

[21] D. Chae, C. Kim, and O. H. Rho, Development of an improved gas-kinetic BGK scheme for inviscid and viscous flows, J. Comput. Phys. **158**, 1 (2000).

[22] J. Jiang and Y. Qian, Implicit gas-kinetic BGK scheme with multigrid for 3D stationary transonic high-Reynolds number flows, Comput. Fluids **66**, 21 (2012).

[23] Y. Sun, C. Shu, C. J. Teo, Y. Wang, and L. M. Yang, Explicit formulations of gas-kinetic flux solver for simulation of incompressible and compressible viscous flows, J. Comput. Phys. **300**, 492 (2015).

[24] L. M. Yang, C. Shu, J. Wu, N. Zhao, and Z. L. Lu, Circular function-based gas-kinetic scheme for simulation of inviscid compressible flows, J. Comput. Phys. **255**, 540 (2013).

[25] L. M. Yang, C. Shu, and J. Wu, A simple distribution function-based gas-kinetic scheme for simulation of viscous

incompressible and compressible flows, J. Comput. Phys. **274**, 611 (2014).
[26] T. Ohwada, On the construction of kinetic schemes, J. Comput. Phys. **177**, 156 (2002).
[27] T. Ohwada and S. Kobayashi, Management of discontinuous reconstruction in kinetic schemes, J. Comput. Phys. **197**, 116 (2004).
[28] P. Asinari and T. Ohwada, Connection between kinetic methods for fluid-dynamic equations and macroscopic finite-difference schemes, Comput. Math. Appl. **58**, 841 (2009).
[29] E. F. Toro, M. Spruce, and W. Speares, Restoration of the contact surface in the HLL-Riemann solver, Shock Wave **4**, 25 (1994).
[30] P. L. Roe, Approximate Riemann solvers, parameter vectors, and difference schemes, J. Comput. Phys. **43**, 357 (1981).
[31] B. van Leer, Towards the ultimate conservative difference scheme V. A second order sequel to Godunov's method, J. Comput. Phys. **32**, 101 (1979).
[32] Y. H. Qian, D. d'Humières, and P. Lallemand, Lattice BGK models for Navier-Stokes equation, EPL **17**, 479 (1992).
[33] S.-S. Kim, C. Kim, O.-H. Rho, and S. K. Hong, Cures for the shock instability: Development of a shock-stable Roe scheme, J. Comput. Phys. **185**, 342 (2003).
[34] K. Qu, C. Shu, and Y. T. Chew, Alternative method to construct equilibrium distribution functions in lattice-Boltzmann method simulation of inviscid compressible flows at high Mach number, Phys. Rev. E **75**, 036706 (2007).
[35] V. Venkatakrishnan, Convergence to steady-state solutions of the Euler equations on unstructured grids with limiters, J. Comput. Phys. **118**, 120 (1995).
[36] Q. Li, Y. L. He, Y. Wang, and W. Q. Tao, Coupled double-distribution-function lattice Boltzmann method for the compressible Navier-Stokes equations, Phys. Rev. E **76**, 056705 (2007).
[37] U. Ghia, K. N. Ghia, and C. T. Shin, High-Re solutions for incompressible flow using the Navier-Stokes equations and a multigrid method, J. Comput. Phys. **48**, 387 (1982).
[38] O. Botella and R. Peyret, Benchmark spectral results on the lid-driven cavity flow, Comput. Fluids **27**, 421 (1998).
[39] P. Jawahar and H. Kamath, A high-resolution procedure for Euler and Navier-Stokes computations on unstructured grids, J. Comput. Phys. **164**, 165 (2000).
[40] A. Haselbacher, J. J. McGuirk, and G. J. Page, Finite volume discretization aspects for viscous flows on mixed unstructured grids, AIAA J. **37**, 177 (1999).
[41] *Numerical Simulation of Compressible Navier-Stokes Flows*, Notes on Numerical Fluid Mechanics Vol. 18, edited by M. O. Bristeau, R. Glowinski, J. Periaux, and H. Viviand (Vieweg and Sonh Braunschweig, Wiesbaden, 1987).
[42] C. B. Lee and S. Wang, Study of the shock motion in a hypersonic shock system/turbulent boundary layer interaction, Exp. Fluids **19**, 143 (1995).
[43] Q. Tang, Y. D. Zhu, X. Chen, and C. B. Lee, Development of second-mode instability in a Mach 6 flat plate boundary layer with two-dimensional roughness, Phys. Fluids **27**, 064105 (2015).
[44] J. H. Miller, PNS Algorithm for Solving Supersonic Flows with Upstream Influences, Retrospective Theses and Dissertations, Iowa State University, Ames, IA, 1997, paper 12012.
[45] J. E. Carter, Numerical solutions of the Navier-Stokes equations for the supersonic laminar flow over a two-dimensional compression corner, NASA Technical Report No. NASA TR R-385, 1972.
[46] C. M. Hung and R. W. MacCormack, Numerical solutions of supersonic and hypersonic laminar compression corner flows, AIAA J. **14**, 475 (1976).